Real-time Low SNR Signal Processing for Nanoparticle Analysis with Deep Neural Networks

Jan Eric Lenssen[1], Anas Toma[2], Albert Seebold[1], Victoria Shpacovitch[3], Pascal Libuschewski[1], Frank Weichert[1], Jian-Jia Chen[2] and Roland Hergenröder[3]

[1]*CS VII - Computer Graphics, TU Dortmund University, Otto-Hahn-Straße 16, 44227 Dortmund, Germany*

[2]*CS XII - Embedded Systems, TU Dortmund University, Otto-Hahn-Straße 16, 44227 Dortmund, Germany*

[3]*Leibniz-Institute for Analytical Science, ISAS e.V., Bunsen-Kirchhoff-Straße 11, 44139 Dortmund, Germany*

Keywords: Nanoparticle Analysis, Deep Learning, Convolutional Neural Network, GPGPU Real Time Processing, Biosensing.

Abstract: In this work, we improve several steps of our PLASMON ASSISTED MICROSCOPY OF NANO-SIZED OBJECTS (PAMONO) sensor data processing pipeline through application of deep neural networks. The PAMONO-biosensor is a mobile nanoparticle sensor utilizing SURFACE PLASMON RESONANCE (SPR) imaging for quantification and analysis of nanoparticles in liquid or air samples. Characteristics of PAMONO sensor data are spatiotemporal blob-like structures with very low SIGNAL-TO-NOISE RATIO (SNR), which indicate particle bindings and can be automatically analyzed with image processing methods. We propose and evaluate deep neural network architectures for spatiotemporal detection, time-series analysis and classification. We compare them to traditional methods like frequency domain or polygon shape features classified by a Random Forest classifier. It is shown that the application of deep learning enables our data processing pipeline to automatically detect and quantify 80 nm polystyrene particles and pushes the limits in blob detection with very low SNRs below one. In addition, we present benchmarks and show that real-time processing is achievable on consumer level desktop GRAPHICS PROCESSING UNITS (GPUs).

1 INTRODUCTION

The effect of SURFACE PLASMON RESONANCE (SPR) is often utilized to study interactions between different types of biomolecules (nucleic acids, peptides, lipids, proteins, etc.) and to determine concentrations and affinity constants of biomolecules in solutions. The high sensitivity of SPR has led to a common use of SPR sensors for real-time measurements of biomolecule binding efficiency. However, the task to quantify individual biological nanoparticles with SPR sensors remained unsolved for a long time.

Recently, the PLASMON ASSISTED MICROSCOPY OF NANO-SIZED OBJECTS (PAMONO) sensor was shown to overcome the limitation of SPR to quantify individual biological nanoparticles (Zybin, 2010; Zybin, 2013; Shpacovitch et al., 2015): single viruses, virus-like particles and other nanoparticles can be detected in suspensions of liquid or air.

Manually analyzing the sensor data and quantify the particles is a time-consuming task. An evaluation of a single data set by an expert with a few hundred particles can take several hours. The application of a highly optimized GENERAL-PURPOSE COMPUTING ON GRAPHICS PROCESSING UNITS (GPGPU) pipeline (Siedhoff, 2016; Libuschewski, 2017) makes it possible to automatically analyze the sensor data and quantifying the nanoparticles in less than three minutes. This enables the real-time measurements of SPR sensors also for the PAMONO sensor. For this automatic analysis, it was shown that it can reliably detect signals with an SNR down to 1.2 and therefore, virus-like and polystyrene particles down to 100 nm in our experiment setup (Siedhoff, 2016; Libuschewski, 2017; Siedhoff et al., 2014). Automatically detecting SPR signals with lower SNR has yet to be accomplished.

In this work, we push the limits of our methods and move towards the goal of detecting particle signals with an SNR below one in PAMONO sensor data by incorporating three different deep neural networks for nanoparticle analysis into our GPGPU

Lenssen, J., Toma, A., Seebold, A., Shpacovitch, V., Libuschewski, P., Weichert, F., Chen, J-J. and Hergenröder, R.
Real-time Low SNR Signal Processing for Nanoparticle Analysis with Deep Neural Networks.
DOI: 10.5220/0006596400360047
In *Proceedings of the 11th International Joint Conference on Biomedical Engineering Systems and Technologies (BIOSTEC 2018) - Volume 4: BIOSIGNALS*, pages 36-47
ISBN: 978-989-758-279-0

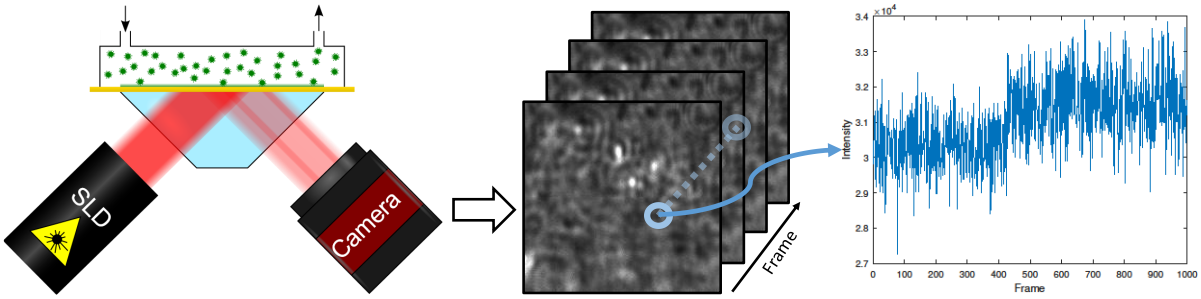

Figure 1: Principle of operation of the PAMONO sensor. It consists of a laser, the flow cell, gold plate, and prism, and the camera, as it is shown in the scheme. Nanoparticles attached to the gold layer result in refractive index changes of the surface, which can be observed by the camera. On the captured image sequences, temporal intensity steps appear on particle binding spots. Figure adapted from (Libuschewski, 2017).

pipeline: a spatiotemporal FULLY CONVOLUTIONAL NETWORK (FCN) (Long et al., 2015), a time-series analysis network (both for detection) and a CONVOLUTIONAL NEURAL NETWORK (CNN) (LeCun et al., 1995) for classification. In our experimental setup, this enables the quantification of 80 nm particles.

We evaluate those methods by performing two different types of experiments: a standalone classification evaluation where we test and compare classification methods on a dedicated benchmark data set and a sensor data experiment where we apply our whole processing pipeline on real sensor data. We show that the proposed methods are able to achieve reliable results for sensor data containing particle signals with an SIGNAL-TO-NOISE RATIO (SNR) below one, and that the pipeline still fulfills the soft real-time property on current GRAPHICS PROCESSING UNITS (GPUs), which means that on average, the data is processed with at least the same speed as the sensor provides it.

2 PAMONO-Biosensor

The PAMONO sensor utilizes a Kretschmann's scheme (Kretschmann, 1971) of plasmon excitation to detect individual particles. In Kretschmann's configuration, as shown in Figure 1, an incident laser beam passes through a glass prism, which is coated with a very thin gold film on one side. This film forms a sensor surface, on which the interactions between biomolecules occur. At a certain angle of incidence (resonance angle), an incidence beam is not reflected and the gold sensor surface is very sensitive to any changes of the refractive index near it. Any changes of the refractive index in close vicinity of the gold interface result in changes of reflection conditions. Thus, any binding of a particle to the gold surface restores the local reflection on the binding spot.

The data characteristic of particle signals in captured images, as shown in Figure 1, is as follows: On places with plasmon excitation through particle bindings, an increase of intensity in the time dimension (intensity step) can be observed in the corresponding pixels. In the spatial dimensions, these pixels form a blob with surrounding wave-like structures. Both variations in intensity are indications for a particle binding and can be detected and analyzed by image processing methods.

3 RELATED WORK

In the following we provide a broad context for nanoparticle analysis in Section 3.1, before we outline the related work for our data processing methods. Analyzing PAMONO sensor data is most related to the field of low SNR blob detection. Therefore, we give a short overview about this subject in Section 3.2.

3.1 Nanoparticle Detection

When comparing SPR-based approaches to study biological nanoparticles, one should highlight the following differences. Conventional SPR sensors deal with the formation of a layer of biomolecules or bioparticles onto a gold sensor surface and harnesses the integral changes of reflectivity conditions to characterize the layer assembly process. In contrast, the PAMONO sensor utilizes local changes of reflectivity to show individual biological nanoparticles. Firstly, the latter issue makes the PAMONO sensor more sensitive in the detection and quantification of biological nanoparticles. Secondary, the PAMONO sensor provides direct information about particle binding events. This helps to obviate complex calculations of particle concentrations based on the thickness of the particle layer

formed onto the sensor surface. Examples of other nanoparticle analysis methods are SURFACE PLASMON RESONANCE IMAGING (SPRi) (Steiner and Salzer, 2001), NANOPARTICLE TRACKING ANALYSIS (NTA) (Dragovic et al., 2011), plaque assay (Dulbecco, 1954), and ENZYME-LINKED IMMUNO-SORBENT ASSAY (ELISA) (Gan and Patel, 2013). A comprehensive overview about the plasmon resonance effect is given by Pattnaik (Pattnaik, 2005).

Most similar to the PAMONO sensor are SPRi sensors which are a wide spread technology that are applied in a large field of applications (Beusink et al., 2008; Chinowsky et al., 2004; Giebel et al., 1999; Naimushin et al., 2003; Scarano et al., 2011). Steiner et al. states that the reason for the advantage of SPRi-based methods is that they show specific bounds of unlabeled molecules under in-situ conditions (Steiner and Salzer, 2001), which also holds for the PAMONO sensor.

3.2 Low SNR Blob Detection

Low SNR blob detection is the most related task to our PAMONO data analysis, as small blob-like structures need to be identified in gray-scale images. Most methods that are comparable to our pipeline can handle an SNR down to four (Cheezum et al., 2001) or two (Smal et al., 2009)

Automatic tumor detection in breast ultrasound images represents a similar task to PAMONO image processing. Moon et al. (Moon et al., 2013) compute features by convolving partial derivatives of a Gaussian distribution with the input images to solve this task and Liu et al. (Liu et al., 2010) apply this method to detect blobs in natural scenes.

Another related task is finding blobs in images from fluorescence microscopy, which was surveyed by Cheezum et al. (Cheezum et al., 2001). It should be noted that for the analyzed tracking tasks, an SNR of four was required for the surveyed algorithms to succeed. For PAMONO signals however, SNRs below one need to be handled.

For live-cell fluorescence microscopy, different spot detection methods have been surveyed by Smal et al. (Smal et al., 2009). It is stated that most classical methods need an SNR of four to work. After presenting algorithms for SNRs down to two, they recommend using supervised machine learning methods for data with low SNR. The deep neural networks used in this work fall under this category.

4 METHODS FOR AUTOMATED NANOPARTICLE DETECTION

The following section details our methods for nanoparticle analysis. First, an overview about the data processing pipeline is given in Section 4.1. In Section 4.2 we describe our deep neural network models for detection and classification and in Section 4.3 we outline our frequency domain methods for comparison. Last, implementation details are given in Section 4.4.

4.1 Image Processing Pipeline - overview

An overview of the image processing pipeline is given in Figure 2. Figure 2a shows the overall detection task with example images: First, a raw image. Second, an image with removed background. Third, detected particle pixels as binary heat map. Finally, generated particle candidates.

Figure 2b shows the existing PAMONO sensor data processing pipeline from previous work (Siedhoff, 2016; Libuschewski, 2017), which makes use of several traditional image processing methods. It consists of the steps preprocessing, detection, particle processing, feature extraction and offline classification. The input is a sequence of sensor images and the output is the particle count and the spatiotemporal coordinates of each particle. The detection step estimates a binary heat map marking possible particle signal positions. After the detection step, the heat map is further processed to generate polygon proposals. These polygons are matched over time to obtain particle candidates that are visible over several frames. Subsequently, polygon features are extracted and the particle candidates are either classified as true particle or artifact/noise in an offline step, using a Random Forest classifier (Breiman, 2001). This pipeline consists of a large number of image processing methods that can be chosen and configured by parameter sets (Libuschewski, 2017). In addition, Siedhoff developed the *SynOpSis* approach to automatically optimize parameter sets towards specific tasks, using synthetic sensor data (Siedhoff, 2016).

Figure 2c shows our proposed processing pipeline, which incorporates novel methods from the field of deep learning: a FULLY CONVOLUTIONAL NETWORK (FCN) and a time-series analysis replace the detection step, a CONVOLUTIONAL NEURAL NETWORK (CNN) online classification replaces the feature extraction and classification step and an additional CNN for online size estimation is added. The online particle size estimation network is able to de-

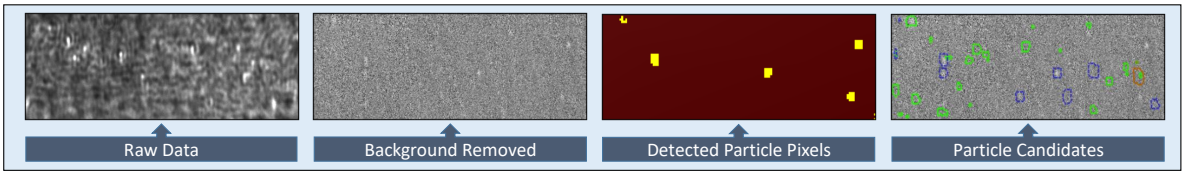

(a) Detection task overview.

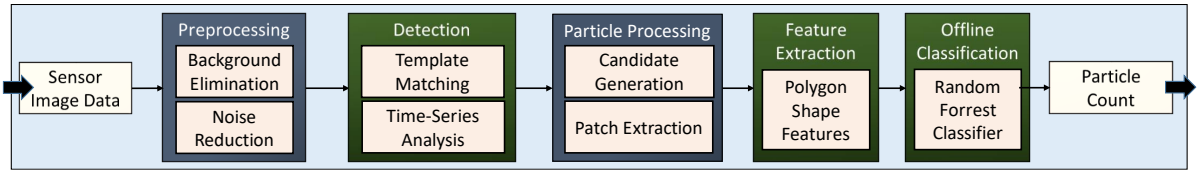

(b) Baseline processing pipeline from previous work.

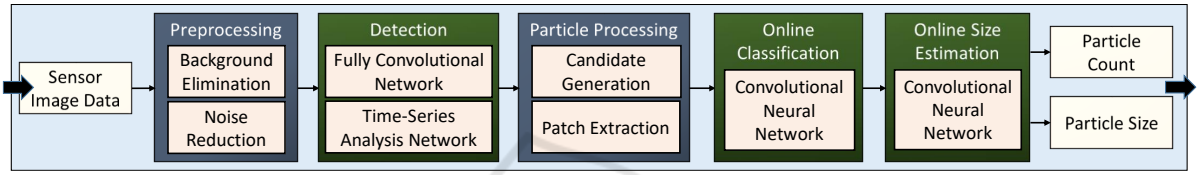

(c) Proposed pipeline with deep neural networks.

Figure 2: An overview of the detection task, the baseline processing pipeline and the proposed processing pipeline. Traditional image processing methods have been replaced by deep neural networks.

rive the size of individual particles, which is part of previous work (Lenssen et al., 2017) but mentioned here for the sake of completeness. All networks are detailed in the following section.

Both pipelines follow the signal model

$$I(x,y,t) = B(x,y) \cdot (T \cdot A)(x,y,t) + N(x,y,t) \quad (1)$$

where I is the sensor image sequence, $T \cdot A$ represents particle and artifact signals and N is additive noise (Siedhoff, 2016). Given the sensor image sequence I, we can approximate the particle and artifact signal $T \cdot A$ by removing the constant-over-time background signal B. This is done by dividing the current image in the sequence by the mean of a set of previous frames. Thus, only the non-constant parts, particle signals, artifacts and noise remains in the images. Then, the detection and classification steps aim to distinguish the particle signal P from artifact A and noise N. In the following sections we provide details of our proposed methods.

4.2 Deep Neural Networks

We present three different neural network architectures for marking pixels that belong to a particle (detection) and to sort out false detections (classification). For the detection task, we present two different approaches which we evaluate against each other. All networks are trained using the cross entropy loss

$$L = -\frac{1}{N} \sum_{i=1}^{N} \mathbf{y}_i \cdot \log \hat{\mathbf{y}}_i, \quad (2)$$

where $\hat{\mathbf{y}}_i$ is the softmax output of the network and $\mathbf{y}_i$ is a binary one-hot vector indicating the correct class. For the detection FCN, we compute the pixel-wise loss and average over the N pixels of all images in one mini-batch while for the remaining networks, the cross entropy is only averaged over all N examples in one mini-batch.

While choosing the neural network architectures, we were driven by two different goals: high accuracy and low inference execution time to maintain the soft real-time property. To achieve the second goal we heavily make use of the two following concepts:

- **Convolutional layers with 1×1 filters**: Strictly speaking, those layers do not perform a convolution but combine the features of each pixel densely to a new set of features while sharing the trained weights over all pixels. In a CNN, some classical convolutional layers can be replaced by those layers to save execution time without losing much accuracy.
- **Feature reduction layers**: As first applied in the *Inception Modules* of the GoogleNet (Szegedy et al., 2015), 1×1 convolution layers can be used to reduce the number of features on each pixel before applying the next layer, which also has shown

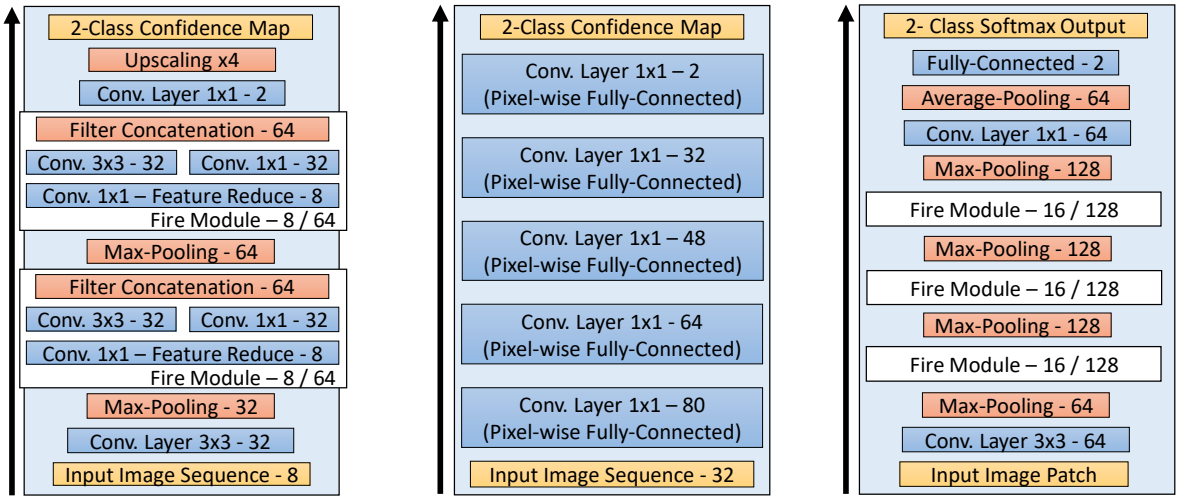

(a) Fully conv. detection network. (b) Time-series analysis network. (c) Particle classification network.

Figure 3: Architectures of our two different detection and our classification network. After the layer description, the number of output feature maps is given for each layer. In each figure, the input is shown on the bottom and the output on the top.

to save execution time without sacrificing much accuracy.

Fully-Convolutional Detection Network. The first detection network combines the ideas of the FCNs from Long et al. (Long et al., 2015) with the efficiency of the inception modules of the GoogleNet (Szegedy et al., 2015) and the spatial-temporal early fusion method mentioned by Karpathy et al. (Karpathy et al., 2014). The architecture is shown in Figure 3a. As network input, we use a stack of 8 subsequent input images from the sensor data stream. Then, the images are processed using scaled-down inception modules, called fire modules, and max pooling. The fire modules, as employed in the SqueezeNet (Iandola et al., 2016), consist of three convolutional layers. First the data is reduced by applying a 1×1 convolutional layer. Then, the number of features is expanded again by another 1×1 and one 3×3 convolutional layer before both results are concatenated along the feature dimension. After three fire modules and max pooling layers, the downscaled feature maps are upscaled to input resolution before computing the pixel-wise loss. As training data, we use stacks of real sensor images together with binary ground truth images that were automatically derived from the manually created ground truth.

Time-Series Analysis Network. The second detection approach classifies the signal in a single pixel over time. This has been accomplished with a 2-class, 5-layer MULTILAYER PERCEPTRON (MLP) classifier. The input time-series consists of 32 signal values, normalized to zero mean and a standard deviation of one. Although this classification network is based on an MLP architecture, it was realized using convolutional layers, due to performance and practical reasons on this particular application. The MLP classifier realized as CNN is shown in Figure 3b. Since the detection runs on an image sequence, the three-dimensional inputs can be used as input for a CNN with 1×1 convolutional layers, which yields a two-dimensional feature map with the same width and height as a single input image. Hence, every layer in this CNN consists of n 1×1 filters, which is equivalent to the densely connected layer with n outputs of the MLP, applied on each pixel, individually.

The time-series classification network was trained exclusively on synthesized data, which is motivated by the fact that it is easier and more accurate to generate realistic pixel time-series than it is to manually label real data. The training data set is composed of 5 000 000 positive and 5 000 000 negative training samples. The negative samples consist of values drawn from a Gaussian distribution $\mathcal{N}(\mu, \sigma^2)$, where means $0.1 \leq \mu \leq 0.9$ and standard deviations $0.005 \leq \sigma \leq 0.25$ are uniformly sampled for each sample. For the positive examples, the same procedure was used and an intensity step with step height depending on target particle size was added on top.

Particle Classification Network. We decided to employ an independent classification CNN (LeCun et al., 1995) after candidate generation to classify between correct detections (particles) and false detections (artifacts and noise). Since this network

is only applied on small signal patches, it allows the application of a deeper network and more filters per layer without destroying the real-time property. Our classification architecture is displayed in Figure 3c. It also makes use of SqueezeNet's FireModules since they have proven to be very fast and effective. As input, the network receives $32\,\text{px} \times 32\,\text{px}$ patches while the output are confidences for two classes. The network is trained using a set of signals that was extracted from real sensor data, as described further in Section 5 and shown in Figure 4.

Particle Size Estimation Network. The particle size estimation is part of the previous work (Lenssen et al., 2017) and is mentioned here for the sake of completeness. It consists of a CNN that simulates regression with classification through binning of the particle sizes. It is trained using synthesized particle patches containing averaged intensity peaks.

4.3 Frequency Domain Analysis

Frequency domain analysis has been used in the literature to detect the abnormalities in medical images (Aljarrah et al., 2015; Woodward et al., 2003). We use it to compare our classification network to a traditional approach on the same task. We extract two types of frequency domain features, spectral and wavelets features, to analyze the texture of the image, because images that contain particles have different texture than images without particles, as shown in Figure 4.

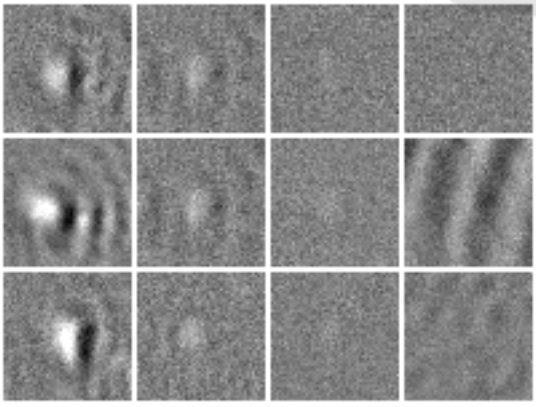

Figure 4: Example patches extracted from the sensor data. The first three columns show signals of 200 nm, 100 nm and 80 nm particles, respectively. The fourth column displays patches containing only noise and artifact signals without particles. The images have been manually enhanced for visualization.

Spectral features can be used to characterize the periodicity of the texture pattern by observing the bursts in Fourier spectrum of the image. The features include the peak value and its location, the mean, the variance, and the distance between the mean and the peak value of the spectrum (Gonzalez and Woods, 2006). Wavelet transform analysis is also used to detect the particles by studying the frequency content of the image in different scales. We use the Haar wavelet transform with 3 scales to produce the coefficients for 10 channels. The energy values of the channels represent the texture features, which can be extracted by calculating the mean magnitude of each channel's coefficients as follows:

$$E = \frac{1}{M \cdot N} \sum_{i=1}^{M} \sum_{j=1}^{N} | \, w(i,j) \, |, \tag{3}$$

where M and N are the dimensions of the channel, and $w(i,j)$ is the wavelet coefficient (Castellano et al., 2004). To classify the patches based on the extracted features a Random Forest classifier was used.

4.4 Implementation Details

The following section presents details and parameters of the training of neural networks, the Random Forest classifiers and the pipeline implementations we used to obtain our results.

Neural Network Training. The FCN and CNNs were trained with TensorFlow (Abadi et al., 2015) using the backpropagation algorithm (Hecht-Nielsen et al., 1988) for gradient estimation and the Adam optimization method (Kingma and Ba, 2014) with an initial step size $\alpha = 0.001$, exponential decay rates $\beta_1 = 0.9$ and $\beta_2 = 0.999$, and $\varepsilon = 10^{-8}$. In contrast, the time-series analysis network was trained with the ADAGRAD optimization method (Duchi et al., 2011) with an initial step of $\alpha = 0.01$ and an exponential decay rate of 0.9. As mini-batch sizes, we used 16 for the FCN detector and 256 for the classification networks. The parameter settings were chosen empirically based on preliminary work.

Training Data Augmentation. In addition to dropout, we applied different data augmentation techniques to further reduce overfitting. For the input of the FCN detector and the CNN classifier we applied small random intensity and contrast modifications as well as random flipping. Intensity and contrast modifications are always applied on the whole image so that relative intensity information is preserved. In addition to that, the $32\,\text{px} \times 32\,\text{px}$ input patches for classification are randomly cropped out of $48\,\text{px} \times 48\,\text{px}$ images. It should be noted that the intensity input of the size estimation network is not

Table 1: Generated patches and captured image sequences used for evaluation with average particle size, number of patches/frames, number of particles and median SNR.

Particle classification data sets	Avg. part. size	# Training images	# Testing images
$Ds1^{Patches}_{100\&200nm}$	100 nm & 200 nm	19344	19344
$Ds2^{Patches}_{80nm}$	80 nm	8308	8308
$Ds3^{Patches}_{80nm}$	80 nm	12916	3700

Sensor experiment data sets	Avg. part. size	# Frames	# Part.	Median SNR
$Ds4_{200nm}$	200 nm	2000	93	2.125
$Ds5_{100nm}$	100 nm	4000	56	1.247
$Ds6_{80nm}$	80 nm	6300	819	0.761
$Ds7_{80nm}$	80 nm	6750	214	0.716
$Ds8_{80nm}$	80 nm	4400	196	0.639

modified, since the absolute intensity holds important information about particle size.

Random Forest Classifier. The Random Forest classifier model has been trained with Weka (Hall et al., 2009). A cross validation parameter tuning (Kohavi, 1995) has been performed to optimize the hyper-parameters of the Random Forest model. The maximum depth of the trees has been optimized from 5 to 20, the number of trees from 100 to 500, and the number of random features from 4 to 9.

Image Processing Pipeline. The GPGPU image processing pipeline, called VIRUS DETECTION WITH OPENCL (VirusDetectionCL), was described and implemented by Libuschewski using OPEN COMPUTING LANGUAGE (OpenCL) (Libuschewski, 2017). For real-time neural network inference, we use DEEP RESOURCE-AWARE OPENCL INFERENCE NETWORKS (deepRacin), an OpenCL-based neural network inference library we created. Using this library, we are able to directly integrate our trained networks into the VirusDetectionCL pipeline and execute them on OpenCL-capable mobile and desktop devices, utilizing the parallel processing power of GPUs.

5 EXPERIMENTS

We provide results for two different types of experiments. First, we solely evaluate the classification network using dedicated classification benchmark data sets, for which examples were given in Figure 4. Subsequently, we use the whole pipeline, including detection and classification networks, to analyze sensor data.

The main focus is on the 80 nm data sets, which have very low SNR. The $\mathrm{SNR}(S,B)$ for a given particle signal S and a given background signal B is calculated according to the definition of Cheezum et al. (Cheezum et al., 2001) as

$$\mathrm{SNR}(S,B) = \frac{|\mu(S) - \mu(B)|}{\sigma(S)}, \tag{4}$$

where S is a multiset of signal values, B a multiset of background values, $\mu(S)$ the average of S, $\mu(B)$ the average of B and $\sigma(S)$ the standard deviation of S.

5.1 Data Set Acquisition

For capturing nanoparticles with the PAMONO sensor we used glass slides covered with a layer of about 50 nm thickness encompassing 5 nm Titanium and approximately 45 nm gold (PHASIS, Switzerland) for the sensor surface. A liquid containing around 10 % of aluminum hydroxide (Nüscoflock, Dr. Nüsgen Chemie, Germany) was employed to cover the gold layer. These gold bearing glass slides were attached to the glass prism with a help of an immersion liquid possessing the same refractive index as the prism. A diode laser (HL6750MG, Thorlabs, Germany) provided an incidence beam with a wavelength $\lambda \approx 675$ nm for illumination of the gold layer through the prism. A 50 mm photographic lens (Rokkor MD, Minolta, Japan) imaged the gold surface onto a 5 Mpx camera (GC2450 Prosilica, Allied Vision, Germany).

Polystyrene nanoparticles (Molecular Probes, Life Technologies, USA) of 200 nm, 100 nm and 80 nm were pumped through the U-shaped flow cell as a suspension in distilled water containing 0.3 % sodium chloride. Image recording speed was 41 fps to 45 fps, but was kept constant during each experiment. For each suspension of 80 nm, 100 nm and 200 nm particles, image sequences were captured, picturing the sensor surface.

The resulting data sets are listed in Table 1. The first three data sets, named $\text{Ds1}^{\text{Patches}}_{\text{100\&200nm}}$, $\text{Ds2}^{\text{Patches}}_{\text{80nm}}$ and $\text{Ds3}^{\text{Patches}}_{\text{80nm}}$ contain extracted patches from the recorded signal, cf. Figure 4, and the subsequent five data sets, named $\text{Ds4}_{\text{200nm}}$, $\text{Ds5}_{\text{100nm}}$, Ds6_{80nm}, Ds7_{80nm} and Ds8_{80nm} are raw sensor image sequences as recorded by the sensor. For all data sets, manually created ground truths are available in which all particle signals were marked by human annotators.

5.2 Standalone Classification Experiment

The first three data sets in Table 1 are benchmark data sets for particle classification. They are used to evaluate the classification CNN and the frequency domain analysis and consist of 48 px × 48 px particle signal patches, which were extracted from sensor signal. Data set $\text{Ds1}^{\text{Patches}}_{\text{100\&200nm}}$ contains disjoint training and testing patches extracted from data sets $\text{Ds4}_{\text{200nm}}$ and $\text{Ds5}_{\text{100nm}}$. Data sets $\text{Ds2}^{\text{Patches}}_{\text{80nm}}$ and $\text{Ds3}^{\text{Patches}}_{\text{80nm}}$ contain patches from data sets Ds6_{80nm} and Ds7_{80nm}. For data set $\text{Ds2}^{\text{Patches}}_{\text{80nm}}$ training and testing images are drawn from both source data sets while for $\text{Ds3}^{\text{Patches}}_{\text{80nm}}$, training images are only extracted from Ds6_{80nm} and testing images from Ds7_{80nm}, thus allowing to evaluate the transferability of the model between different measurements. In all 3 generated data sets, training and testing data are disjoint and class-balanced, allowing to use accuracy as quality measure.

We applied two different methods on these data sets: the CNN classifier called $\text{M}^{\text{CNN-Cl}}$ and the frequency domain analysis with Random Forest classifier called $\text{M}^{\text{FDA}}_{\text{RF}}$.

5.3 Sensor Data Experiment

We evaluate the whole processing pipeline by comparing the results (proposed particles that were positively classified) to the manually created ground truth. Data set Ds6_{80nm} was used for training the detector and classification network. The trained models were tested on data sets $\text{Ds4}_{\text{200nm}}$, $\text{Ds5}_{\text{100nm}}$, Ds7_{80nm} and Ds8_{80nm}.

As quality measures, precision, recall and the F_1-score (Powers, 2011) are used. The F_1-score is defined as a balance between precision and recall:

$$\text{F}_1 = \frac{2 \cdot \text{precision} \cdot \text{recall}}{\text{precision} + \text{recall}}. \quad (5)$$

We differentiate between results obtained by applying the detection step only and that obtained by detecting and classifying. Ideally, the detector provides high recall while the classification is able to sort out false positives without sorting out too many true positives. Therefore, we applied and compared five different methods:

- $\text{M}^{\text{Baseline}}$: baseline pipeline (previous work),
- $\text{M1}^{\text{FCN-Det}}$: the FCN detector without classification,
- $\text{M2}^{\text{FCN-Det}}_{\text{CNN-Cl}}$: the FCN detector with CNN classification,
- $\text{M3}^{\text{TS-Det}}$: the time-series analysis network without classification,
- $\text{M4}^{\text{TS-Det}}_{\text{CNN-Cl}}$: the time-series detection network with CNN classification.

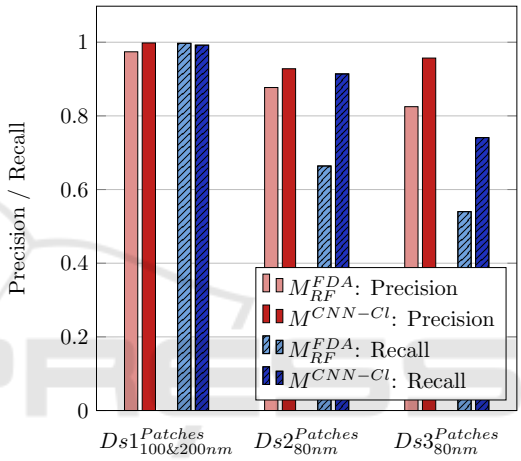

Figure 5: Precision and recall of the classification results. Values are given for the positive class. Mostly, precision is higher than recall, as preferred. The $\text{M}^{\text{CNN-Cl}}$ method provides stronger results.

Table 2: Classification accuracy results for the generated data sets and the two methods: frequency domain analysis plus Random Forest classifier $\text{M}^{\text{FDA\&RF}}$ and CNN classification $\text{M}^{\text{CNN-Cl}}$.For each row, the bold value shows the best result.

Data set / method	$\text{M}^{\text{FDA}}_{\text{RF}}$	$\text{M}^{\text{CNN-Cl}}$
$\text{Ds1}^{\text{Patches}}_{\text{100\&200nm}}$	0.985	**0.995**
$\text{Ds2}^{\text{Patches}}_{\text{80nm}}$	0.786	**0.922**
$\text{Ds3}^{\text{Patches}}_{\text{80nm}}$	0.713	**0.854**

6 RESULTS AND DISCUSSION

In the following Sections 6.1 and 6.2, we present and discuss results for the two different classes of experiments that were described in Section 5. Then, we provide benchmark results for our pipeline in Section 6.3.

Table 3: Detection results evaluated for the baseline method and the four presented methods on five data sets. Quality measures are given as precision, recall and F_1-score. For each row, the bold value shows the best result.

Data set / method		M^{Baseline}	$M1^{\text{FCN-Det}}$	$M2^{\text{FCN-Det}}_{\text{CNN-Cl}}$	$M3^{\text{TS-Det}}$	$M4^{\text{TS-Det}}_{\text{CNN-Cl}}$
$Ds4_{200nm}$	Precision	0.909	0.888	0.908	**0.933**	0.933
	Recall	0.787	0.763	0.742	**0.903**	0.892
	F_1-score	0.844	0.821	0.817	**0.918**	0.918
$Ds5_{100nm}$	Precision	0.769	0.814	0.842	0.235	**0.938**
	Recall	0.798	0.857	0.857	**0.929**	0.803
	F_1-score	0.783	0.835	0.810	0.375	**0.865**
$Ds6_{80nm}$	Precision	0.410	0.782	**0.877**	0.098	0.887
	Recall	0.492	0.715	0.677	**0.967**	0.506
	F_1-score	0.448	0.747	**0.764**	0.177	0.644
$Ds7_{80nm}$	Precision	0.330	0.347	**0.840**	0.025	0.829
	Recall	0.549	0.795	0.707	**0.967**	0.428
	F_1-score	0.412	0.483	**0.768**	0.049	0.564
$Ds8_{80nm}$	Precision	0.053	0.258	**0.801**	0.017	0.729
	Recall	0.561	0.782	0.553	**0.970**	0.355
	F_1-score	0.097	0.388	**0.655**	0.033	0.478

6.1 Standalone Particle Classification

The results for the standalone particle classification are shown in Table 2. It shows classification accuracy for the two presented classification methods $M^{\text{FDA}}_{\text{RF}}$ and $M^{\text{CNN-Cl}}$.

We observe nearly the same accuracy of both motehods on the easier $Ds1^{\text{Patches}}_{100\&200nm}$ data set. However, the results on the 80 nm data sets $Ds2^{\text{Patches}}_{80nm}$ and $Ds3^{\text{Patches}}_{80nm}$ show that the $M^{\text{CNN-Cl}}$ method outperforms the $M^{\text{FDA}}_{\text{RF}}$ method on harder tasks. The difference in accuracy between data sets $Ds2^{\text{Patches}}_{80nm}$ and $Ds3^{\text{Patches}}_{80nm}$ show that transferring the model to a different measurement is possible but leads, in this case, to a significant decrease in accuracy. However, we show that even the transferred classification model is able to improve the detection results provided in the next section.

For more insight, we also detail precision and recall of each approach and data set in Figure 5. In general, the precision is higher than the recall, which is also what is preferred most of the time. In addition, the $M^{\text{CNN-Cl}}$ method shows better results than the $M^{\text{FDA}}_{\text{RF}}$ method in both criteria. All in all, these results led us to the decision to use the $M^{\text{CNN-Cl}}$ method together with our detection networks for our sensor data experiments that are presented in the following section.

6.2 Sensor Data Experiment

The results for the sensor data experiment are shown in Table 3. The quality measures precision, recall and F_1-score are provided for the baseline method and the four presented methods on five data sets. The best results of each experiment are printed bold.

First, it should be noted that $Ds6_{80nm}$ was used to train the $M1^{\text{FCN-Det}}$ detector and to extract the training data for data set $Ds3^{\text{Patches}}_{80nm}$, which was used to train the applied $M^{\text{CNN-Cl}}$ classifier. Therefore, the results of methods $M1^{\text{FCN-Det}}$, $M2^{\text{FCN-Det}}_{\text{CNN-Cl}}$ and $M4^{\text{TS-Det}}_{\text{CNN-Cl}}$ for $Ds6_{80nm}$ are training scores. The other data sets were not seen during training and used to calculate the testing score. Since the time-series classification network was trained using synthetic data, all results of method $M3^{\text{TS-Det}}$ are test results.

The evaluation shows that nearly all our methods outperform the baseline method M^{Baseline} by a large margin. The $M3^{\text{TS-Det}}$ and $M4^{\text{TS-Det}}_{\text{CNN-Cl}}$ methods provide strong results on data sets with a median SNR above one. For data set $Ds4_{200nm}$, the classifier is not even needed to sort out false positives. For data sets with a median SNR below one however, the resulting time-series detection network shows very high sensitivity, resulting in low precision in order to find most true positives. Therefore, it heavily relies on the classifier to sort out false positives consisting of noise and artifacts. For these data sets, the combination of the FCN detector and the CNN classifier, method $M2^{\text{FCN-Det}}_{\text{CNN-Cl}}$, proves to be the strongest method. It achieves a precision above 0.8 on all three data sets, thus having a low

number of false positives. This indicates that, especially for low SNR signals, the local spatial information is important to perform reliable detection and that time-series information of one pixel is not enough to distinguish between artifact and particle signals. The recall, despite being not optimal, is sufficient for a lot of tasks, in which the existence and size distributions of particles should be derived. The worse results for this method on data sets $\mathrm{Ds4}_{200\mathrm{nm}}$ and $\mathrm{Ds5}_{100\mathrm{nm}}$ is easily explained by the fact that the networks were not trained with images containing 100 nm and 200 nm particles.

6.3 Performance Analysis

We profiled the proposed processing pipeline as well as each deep neural network on an NVIDIA GeForce GTX 1080 Ti. For whole pipeline application, we achieve 15.296 ms per frame (65.4 fps) when using the $\mathrm{M4}^{\text{TS-Det}}_{\text{CNN-Cl}}$ method and 23.478 ms (42.5 fps) when using the $\mathrm{M4}^{\text{TS-Det}}_{\text{CNN-Cl}}$ method. Applying the FCN detector on one image takes 0.827 ms while the time-series analysis network is slower and takes 9.675 ms. The classification CNN takes 0.119 ms per patch classification. All measurements were performed on data set $\mathrm{Ds7}_{80\mathrm{nm}}$, which has 6750 images with a resolution of $880\,\mathrm{px} \times 115\,\mathrm{px}$.

7 CONCLUSIONS

In this work, we proposed additional deep neural network methods for the PAMONO sensor data analysis pipeline. We showed that through this extensions, the detection of blobs with a median SNR below one is possible. All in all, we achieved results on signals with a median SNR of 0.7 that were previously reached on data sets with a median SNR of 1.25.

Our pipeline, consisting of detection and classification networks, was able to achieve sufficiently high results for most real world nanoparticle analysis applications of the PAMONO sensor while fulfilling the soft real-time property on desktop GPUs. We are able to successfully analyze suspensions containing 80 nm polystyrene particles, given our current sensor experiment setup. Detecting even smaller particles in the future requires either the improvement of the data (with higher SNR for the same particle size) or the capability of the detection pipeline to handle even lower SNR. In addition, we aim to bring the pipeline to embedded GPUs, to further move towards the goal of small, mobile nanoparticle analysis with the PAMONO sensor.

ACKNOWLEDGMENTS

This work has been supported by DEUTSCHE FORSCHUNGSGEMEINSCHAFT (DFG) within the Collaborative Research Center SFB 876 *Providing Information by Resource-Constrained Analysis*, project B2.

REFERENCES

Abadi, M., Agarwal, A., Barham, P., Brevdo, E., Chen, Z., Citro, C., Corrado, G. S., Davis, A., Dean, J., Devin, M., Ghemawat, S., Goodfellow, I., Harp, A., Irving, G., Isard, M., Jia, Y., Jozefowicz, R., Kaiser, L., Kudlur, M., Levenberg, J., Mané, D., Monga, R., Moore, S., Murray, D., Olah, C., Schuster, M., Shlens, J., Steiner, B., Sutskever, I., Talwar, K., Tucker, P., Vanhoucke, V., Vasudevan, V., Viégas, F., Vinyals, O., Warden, P., Wattenberg, M., Wicke, M., Yu, Y., and Zheng, X. (2015). Tensorflow: Large-scale machine learning on heterogeneous systems.

Aljarrah, I., Toma, A., and Al-Rousan, M. (2015). An automatic intelligent system for diagnosis and confirmation of johne's disease. *Int. J. Intell. Syst. Technol. Appl.*, 14(2):128–144.

Beusink, J. B., Lokate, A. M. C., Besselink, G. A. J., Pruijn, G. J. M., and Schasfoort, R. B. M. (2008). Angle-scanning spr imaging for detection of biomolecular interactions on microarrays. *Biosensors and Bioelectronics*, 23(6):839–844.

Breiman, L. (2001). Random forests. *Machine Learning*, 45(1):5–32.

Castellano, G., Bonilha, L., Li, L. M., and Cendes, F. (2004). Texture analysis of medical images. *Clinical Radiology*, 59(12):1061–1069.

Cheezum, M. K., Walker, W. F., and Guilford, W. H. (2001). Quantitative comparison of algorithms for tracking single fluorescent particles. *Biophysical Journal*, 81(4):2378–2388.

Chinowsky, T. M., Mactutis, T., Fu, E., and Yager, P. (2004). Optical and electronic design for a high-performance surface plasmon resonance imager. In *Optical Technologies for Industrial, Environmental, and Biological Sensing*, pages 173–182.

Dragovic, R. A., Gardiner, C., Brooks, A. S., Tannetta, D. S., Ferguson, D. J., Hole, P., Carr, B., Redman, C. W., Harris, A. L., Dobson, P. J., Harrison, P., and Sargent, I. L. (2011). Sizing and phenotyping of cellular vesicles using nanoparticle tracking analysis. *Nanomedicine: Nanotechnology, Biology and Medicine*, 7(6):780 – 788.

Duchi, J., Hazan, E., and Singer, Y. (2011). Adaptive subgradient methods for online learning and stochastic optimization. *Journal of Machine Learning Research*, 12(Jul):2121–2159.

Dulbecco, R. (1954). Plaque formation and isolation of pure lines with poliomylitis viruses. *Journal of Experimental Medicine*, 99(2):167–182.

Gan, S. D. and Patel, K. R. (2013). Enzyme immunoassay and enzyme-linked immunosorbent assay. *The Journal of Investigative Dermatology*, 133(9):1–3.

Giebel, K.-F., Bechinger, C. S., Herminghaus, S., Riedel, M., Leiderer, P., Weiland, U. M., and Bastmeyer, M. (1999). *Imaging of Cell/Substrate Contacts of Living Cells with Surface Plasmon Resonance Microscopy*. Bibliothek der Universität Konstanz, Konstanz, Germany.

Gonzalez, R. C. and Woods, R. E. (2006). *Digital Image Processing (3rd Edition)*. Prentice-Hall, Inc, Upper Saddle River, NJ, USA.

Hall, M., Frank, E., Holmes, G., Pfahringer, B., Reutemann, P., and Witten, I. H. (2009). The weka data mining software: An update. *ACM SIGKDD Explorations Newsletter*, 11(1):10–18.

Hecht-Nielsen, R. et al. (1988). Theory of the backpropagation neural network. *Neural Networks*, 1(Supplement-1):445–448.

Iandola, F. N., Moskewicz, M. W., Ashraf, K., Han, S., Dally, W. J., and Keutzer, K. (2016). Squeezenet: Alexnet-level accuracy with 50x fewer parameters and <1mb model size. *CoRR*, abs/1602.07360.

Karpathy, A., Toderici, G., Shetty, S., Leung, T., Sukthankar, R., and Li, F.-F. (2014). Large-scale video classification with convolutional neural networks. In *2014 IEEE Conference on Computer Vision and Pattern Recognition, CVPR 2014, Columbus, OH, USA, June 23-28, 2014*, pages 1725–1732.

Kingma, D. P. and Ba, J. (2014). Adam: A method for stochastic optimization. In *Proceedings of the 3rd International Conference on Learning Representations (ICLR)*.

Kohavi, R. (1995). *Wrappers for Performance Enhancement and Oblivious Decision Graphs*. PhD thesis, Stanford University, Department of Computer Science, Stanford University.

Kretschmann, E. (1971). The determination of the optical constants of metals by excitation of surface plasmons. *European Physical Journal A*, 241(4):313–324.

LeCun, Y., Bengio, Y., et al. (1995). Convolutional networks for images, speech, and time series. *The handbook of brain theory and neural networks*, 3361(10):1995.

Lenssen, J. E., Shpacovitch, V., and Weichert, F. (2017). Real-time virus size classification using surface plasmon pamono resonance and convolutional neural networks. In Maier-Hein, K. H., Deserno, T. M., Handels, H., and Tolxdorff, T., editors, *Bildverarbeitung für die Medizin 2017*, Informatik Aktuell, pages 98–103. Springer, Berlin, Germany and Heidelberg, Germany.

Libuschewski, P. (2017). *Exploration of Cyber-Physical Systems for GPGPU Computer Vision-Based Detection of Biological Viruses*. PhD thesis, TU Dortmund, Dortmund, Germany.

Liu, J., White, J. M., and Summers, R. M. (2010). Automated detection of blob structures by hessian analysis and object scale. In *Image Processing (ICIP). 17th IEEE International Conference on*, pages 841–844.

Long, J., Shelhamer, E., and Darrell, T. (2015). Fully convolutional networks for semantic segmentation. In *IEEE Conference on Computer Vision and Pattern Recognition, CVPR 2015, Boston, MA, USA, June 7-12, 2015*, pages 3431–3440.

Moon, W. K., Shen, Y.-W., Bae, M. S., Huang, C.-S., Chen, J.-H., and Chang, R.-F. (2013). Computer-aided tumor detection based on multi-scale blob detection algorithm in automated breast ultrasound images. *Medical Imaging. IEEE Transactions on*, 32(7):1191–1200.

Naimushin, A. N., Soelberg, S. D., Bartholomew, D. U., Elkind, J. L., and Furlong, C. E. (2003). A portable surface plasmon resonance (spr) sensor system with temperature regulation. *Sensors and Actuators B: Chemical*, 96(1-2):253–260.

Pattnaik, P. (2005). Surface plasmon resonance: Applications in understanding receptor-ligand interaction. *Applied Biochemistry and Biotechnology*, 126(2):79–92.

Powers, D. M. W. (2011). Evaluation: From precision, recall and f-measure to roc., informedness, markedness & correlation. *Journal of Machine Learning Technologies*, 2(1):37–63.

Scarano, S., Ermini, M. L., Mascini, M., and Minunni, M. (2011). Surface plasmon resonance imaging for affinity-based sensing: An analytical approach. In *BioPhotonics. International Workshop on*, pages 957–966.

Shpacovitch, V., Temchura, V., Matrosovich, M., Hamacher, J., Skolnik, J., Libuschewski, P., Siedhoff, D., Weichert, F., Marwedel, P., Müller, H., Überla, K., Hergenröder, R., and Zybin, A. (2015). Application of surface plasmon resonance imaging technique for the detection of single spherical biological submicrometer particles. *Analytical Biochemistry: Methods in the Biological Sciences*, 486:62–69.

Siedhoff, D. (2016). A parameter-optimizing model-based approach to the analysis of low-snr image sequences for biological virus detection. phd, Universität Dortmund. Publikation.

Siedhoff, D., Libuschewski, P., Weichert, F., Zybin, A., Marwedel, P., and Müller, H. (2014). Modellierung und optimierung eines biosensors zur detektion viraler strukturen. In Deserno, T. M., Handels, H., Meinzer, H.-P., and Tolxdorff, T., editors, *Bildverarbeitung für die Medizin (BVM)*, Informatik Aktuell, pages 108–113. Springer, Berlin, Germany and Heidelberg, Germany.

Smal, I., Loog, M., Niessen, W., and Meijering, E. (2009). Quantitative comparison of spot detection methods in live-cell fluorescence microscopy imaging. In *Biomedical Imaging: From Nano to Macro. IEEE International Symposium on*, pages 1178–1181.

Steiner, G. and Salzer, R. (2001). Biosensors based on spr imaging. In Tübingen, U., editor, *2. BioSensor Symposium*, Tübingen, Germany. Universität Tübingen.

Szegedy, C., Liu, W., Jia, Y., Sermanet, P., Reed, S., Anguelov, D., Erhan, D., Vanhoucke, V., and Rabinovich, A. (2015). Going deeper with convolutions. In *IEEE Conference on Computer Vision and Pattern Recognition (CVPR)*, pages 1–9. IEEE.

Woodward, R. M., Wallace, V. P., Arnone, D. D., Linfield, E. H., and Pepper, M. (2003). Terahertz pulsed imaging of skin cancer in the time and frequency domain. *Journal of Biological Physics*, 29(2-3):257–259.

Zybin, A. (2010). DE patent 10,2009,003,548 A1: Verfahren zur hochaufgelösten erfassung von nanopartikeln auf zweidimensionalen messflächen.

Zybin, A. (2013). US patent 8,587,786 B2: Method for high-resolution detection of nanoparticles on two-dimensional detector surfaces.